




# Electrical conductivity of copper under ultrahigh pressure and temperature conditions by both experiments and first-principles simulations

Bo Gan (甘波)<sup>1</sup>, Jun Li (李俊)<sup>2</sup>, Junjie Gao (高俊杰)<sup>2</sup>, Qiru Zeng (曾琪茹)<sup>1</sup>, Wenhao Song (宋文豪)<sup>1</sup>,  
Yukai Zhuang (庄毓凯)<sup>1</sup>, Yingxin Hua (华颖鑫)<sup>2</sup>, Qiang Wu (吴强)<sup>2</sup>, Gang Jiang (蒋刚)<sup>1</sup>,  
Yuan Yin (尹远)<sup>3,\*</sup> and Youjun Zhang (张友君)<sup>1,4,†</sup>

<sup>1</sup>*Institute of Atomic and Molecular Physics, Sichuan University, Chengdu 610065, China*

<sup>2</sup>*National Key Laboratory for Shock Wave and Detonation Physics, Institute of Fluid Physics, CAEP, Mianyang 621900, China*

<sup>3</sup>*State Key Laboratory of Ore Deposit Geochemistry, Institute of Geochemistry, Chinese Academy of Sciences, Guiyang 550081, China*

<sup>4</sup>*Key Laboratory of High Energy Density Physics and Technology of Ministry of Education, Sichuan University, Chengdu 610065, China*



(Received 25 November 2023; revised 29 January 2024; accepted 23 February 2024; published 15 March 2024)

Copper (Cu) is ubiquitously utilized in industry owing to its exceptional electrical conductivity and serves as a standard material in shock compression experiments. However, a comprehensive understanding of the electrical and thermal transport properties of Cu under extreme pressure-temperature ( $P$ - $T$ ) conditions remains a significant challenge due to limited experiments and theoretical constraints. In this work, we have developed a robust methodology for achieving high-quality electrical resistivity measurements of transition metals at ultrahigh  $P$ - $T$  conditions under shock compression. We conducted electrical resistivity measurements on Cu utilizing a four-probe method in a diamond anvil cell up to 50 GPa at ambient temperature, and in a two-stage light-gas gun up to 118 GPa and 1800 K. Simultaneously, we computed the electrical and thermal conductivity of face-centered cubic (fcc) Cu over a wide  $P$ - $T$  range using first-principles molecular dynamics simulations. Notably, our experimental and theoretical results are overall consistent with each other. Our results reveal that the electrical resistivity of fcc Cu diminishes with increasing pressure and displays a linear augmentation with rising temperature. The relationship between the electrical resistivity of fcc Cu and temperature can be described by the Bloch-Grüneisen formula, indicating that electron-phonon scattering governs its electrical conductivity.

DOI: [10.1103/PhysRevB.109.115129](https://doi.org/10.1103/PhysRevB.109.115129)

## I. INTRODUCTION

The electrical conductivity of transition metals under extreme pressure-temperature ( $P$ - $T$ ) conditions is of significant interest in condensed matter physics and has important applications in high-energy density physics, high-pressure science, and planetary sciences [1–5]. Over the past four decades, numerous experimental and theoretical efforts have been undertaken to investigate the electrical conductivity of metals in the solid and liquid states [6,7]. Theoretical simulation techniques, including density functional theory (DFT), first-principles molecular dynamics (FPMD), Korringa-Kohn-Rostoker Green function method with coherent potential approximation, nonequilibrium *ab initio* molecular dynamics, real-time formalism of time-dependent DFT, and other methods have been extensively applied to model electrical conductivity and elucidate the effects of pressure and temperature on electronic structure [8–17]. However, some theoretical approaches often yield divergent predictions because accurately modeling the electron-phonon interactions under extreme conditions remains challenging [18–25]. Consequently, reliable experimental measurements of the electrical transport properties of metals at high  $P$ - $T$  are critically

necessary to provide benchmarking data for simulations and advance understanding in this domain.

High  $P$ - $T$  conditions can be generated in the laboratory employing both static and dynamic compression techniques. Static techniques, including large-volume presses (LVPs) and diamond-anvil cells (DACs), have been extensively used to quantify electrical conductivity. However, LVPs are typically constrained to pressures of  $\sim 25$  GPa and temperatures  $< 2500$  K due to limitations on their loading capacity [26–38]. Laser-heated DACs (LH-DACs) extend the accessible  $P$ - $T$  range of static techniques to a few Mbar and 5000–6000 K [39–44], enabling electrical conductivity measurements up to  $\sim 170$  GPa and  $\sim 3500$  K [5,45–55]. Nevertheless, probing the extreme  $P$ - $T$  conditions found in planetary cores requires accessing even higher pressures and temperatures.

Dynamic compression techniques harnessing multistage gas guns or high-powered lasers to generate strong shock waves provide a means to achieve ultrahigh  $P$ - $T$  conditions and conduct electrical resistivity measurements beyond 200 GPa and 5000 K. Prior investigations into electrical resistivities of insulators [56–62], liquids [63–74], and metals [75–84] under shock loading have employed various target designs. However, measurements on metals have faced challenges attributable to the skin depth effect, wherein the current is confined near the surface rather than permeating the entire sample thickness [85]. Meanwhile, increased sample thickness introduces greater uncertainties in resistivity

\*yinyuan@mail.gyg.ac.cn

†zhangyoujun@scu.edu.cn

determination due to their diminished initial resistance. Recent advances by Crum *et al.* [85] involved the use of thinly deposited metal films as samples to mitigate the skin depth effect. This approach not only improved the measurement accuracy by ensuring a more uniform current distribution but also aligned well with impedance-matched electronic systems tailored for the particularities of resistivity experiments under shock compression.

Cu is a widely used transition metal with extensive applications in electronic industries [86] and serves as a standard material commonly employed in shock wave physics. Notably, the investigation of its electrical resistivity at high  $P$ - $T$  conditions has attracted substantial attention. Matula [87] consolidated the resistivity data of Cu from cryogenic temperatures up to above its melting point at 1357 K at ambient pressure utilizing Bloch-Grüneisen models. The resistivity of Cu has additionally been quantified under static and dynamic compressions up to  $\sim 20$  GPa and 2100 K [33,34,80,88–90]. Some previous experiments conducted under dynamic compression have revealed a significant increase in its resistivity as pressure rises [80,90]. Conversely, other experiments under static compression exhibited a contrasting trend [33,34]. First-principles simulations have also been employed to understand the resistivity of Cu at high  $P$ - $T$ , but these simulations were conducted at relatively low pressures and temperatures [88,91]. More recently, the resistivity was estimated up to 100 GPa and 1350 K, utilizing a combination of Bloch-Grüneisen theory, the Debye model, and a statistical moment method (SMM) [92]. These findings indicate that an increase in temperature leads to a rise in the resistivity of Cu, while elevated pressure results in its reduction. However, the pressure dependence predicted by the SMM exhibited significant deviation from both the first-principles simulations and the static high-pressure experiments. As a result, significant uncertainties persist due to the limited data available at high  $P$ - $T$  conditions, disparities between measurement techniques, and unverified reliability of predictive models. These challenges represent a significant impediment to a comprehensive understanding of the electrothermal transport properties of Cu under extreme conditions.

In this study, we measured the electrical resistivity of Cu up to  $\sim 120$  GPa and  $\sim 1800$  K utilizing both DAC and two-stage light-gas gun techniques, supported by FPMD simulations. The sample assemblies were strategically modified to mitigate the influence of the skin depth and gap effects inherent in dynamic compression. The obtained results exhibit excellent agreement with the FPMD simulations, demonstrating adherence to the Bloch-Grüneisen formula. This conformity suggests the prevalence of electron-phonon scattering as the primary contributor to the electrical resistivity of Cu under the current  $P$ - $T$  conditions, with resistivity saturation exhibiting negligible influence.

## II. METHODS

### A. Electrical resistivity measurements of Cu in a DAC

The electrical resistivity of Cu was measured up to a static pressure of 50 GPa at room temperature utilizing a four-probe configuration within a DAC equipped with 300  $\mu\text{m}$  flat

culet diamonds (Fig. S1 in the Supplemental Material [93]). A T-301 steel gasket was preindented to a pressure of  $\sim 25$  GPa. Within the preindented region, a culet-sized hole ( $\sim 80\%$ ) was laser-drilled and subsequently filled with cubic boron nitride (cBN) powder, serving as an insulating gasket insert. The cBN was compressed to  $\sim 20$  GPa before laser-drilling a sample chamber with a diameter of  $\sim 100$   $\mu\text{m}$  diameter. A 5- $\mu\text{m}$ -thick Cu foil (with 99.9% purity) was shaped into a disc with a diameter of  $\sim 40$   $\mu\text{m}$ . This sample was placed into the prepared sample chamber, along with dry  $\text{SiO}_2$  as the pressure-transmitting medium, and ruby chips for *in situ* pressure determination via fluorescence shifts [94]. Four platinum (Pt) electrical leads were connected to the Cu sample. Sample resistance was obtained using Ohm's law, applying a 100 mA direct current (DC) with a DC source (Keithley 6221) and measuring voltage with a nanovoltmeter (Keithley 2182A).

Three separate runs were conducted at high pressure and room temperature. Previous work has demonstrated that the shape and size of the sample and electrodes remained largely unaltered during decompression [45,95]. Thus, we collected the resistance of Cu during decompression. The electrical resistivity ( $\rho$ ) of Cu at high pressure was then derived from the measured resistance ( $R$ ) as

$$\rho = \rho_0 \frac{R}{R_0} \left( \frac{V}{V_0} \right)^{1/3}, \quad (1)$$

where  $V$  is the pressure-dependent volume of Cu calculated from its equation of state (EoS) [96,97];  $\rho_0$ ,  $R_0$ , and  $V_0$  are the electrical resistivity, resistance, and volume at ambient conditions, respectively, with  $\rho_0 = 1.725 \times 10^{-8} \Omega \text{ m}$  [87]. Uncertainty was estimated based on the methods for error analysis [5], yielding resistivity errors generally  $< 5\%$ . Multiple runs enabled consistency verification and precision resistivity determinations up to 50 GPa at room temperature.

### B. Electrical resistivity measurements of Cu in a two-stage light-gas gun

The electrical resistivity of Cu at high  $P$ - $T$  conditions was measured up to 118 GPa and  $\sim 1800$  K using the four-probe technique under dynamic compression in a two-stage light-gas gun [98]. The experimental setup is shown in Fig. 1(a). A DC pulse power supply applied a constant current through the sample, and an oscilloscope recorded the voltage. Input current was monitored using a Rogowski coil within the supply. Five 100 m $\Omega$  low-temperature coefficient resistors were connected in parallel to check the power discharge characteristics (Fig. S2(a) in the Supplemental Material [93]). The result shows a quasicontant between 0 and 400 A current over  $\sim 60$   $\mu\text{s}$  (Fig. S2(b) in the Supplemental Material [93]), ensuring a constant current during shock loading (Fig. S2(c) in the Supplemental Material [93]).

High  $P$ - $T$  conditions were generated by hypervelocity planar impact in the two-stage light-gas gun with a 25 mm bore tube at Sichuan University. The Cu flyer (24 mm diameter and 2 mm thickness) was accelerated to velocities up to several km/s prior to impact with the target. The impact velocity ( $w$ ) was measured by an electromagnetic method within  $\sim 0.5\%$  uncertainty [99]. Meanwhile, the electromagnetic signal was

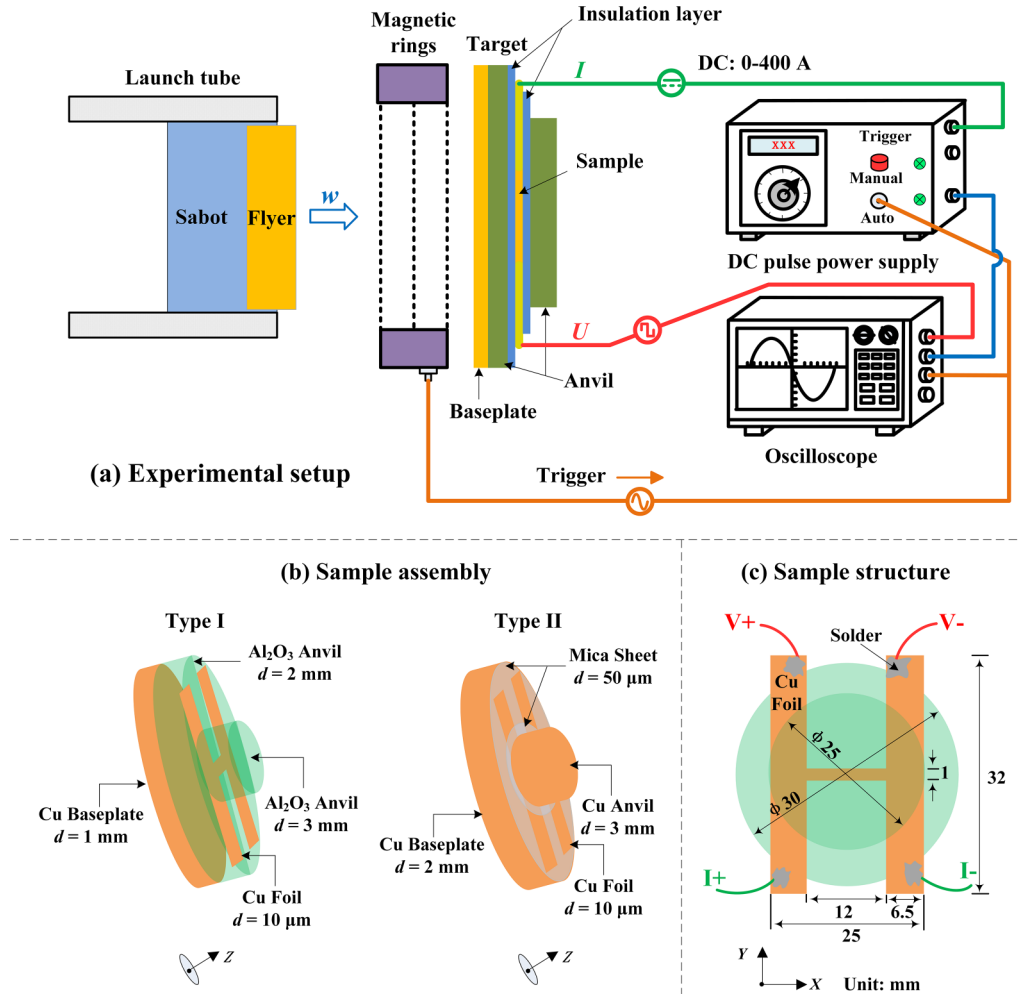


FIG. 1. Experimental configuration for the electrical resistivity measurements of Cu under shock compression. (a) Schematic of the experimental setup. Triggering of the power supply and oscilloscope is synchronized by the induced voltage from the passage of the high-velocity flyer through the magnetic ring. Measuring the transient voltage response under an applied constant current allows the determination of the electrical resistance evolution induced by shock compression of the sample. (b) Schematic of the sample assembly. The sample assembly consists of the Cu foil sample sandwiched between two anvils with insulating layers. Two configurations were used:  $\text{Al}_2\text{O}_3$  as both anvils and insulators (Type I), and Cu anvils with mica insulation (Type II). (c) Schematic of the sample structure. The length, width, and thickness of the Cu sample are 12 mm, 1 mm, and 10  $\mu\text{m}$ , respectively.

also used to trigger the power supply to discharge at  $\sim 7\text{--}14$   $\mu\text{s}$  before impact.

For shock experiments, a 10- $\mu\text{m}$ -thick Cu foil (99.9% purity) was cut into an H-shaped structure, with the sample comprising a  $12 \times 1$  mm rectangle. Two  $6.5 \times 32$  mm Cu strips seamlessly connected at each end of the sample, enabling four electrodes to be soldered. Voltage and current leads were situated on opposite sample sides, with the voltage leads in closer sample proximity [Fig. 1(c)]. Each lead was soldered to a coaxial cable center wire, while the shield was grounded. Epoxy resin was used to electrically isolate the exposed leads from the steel target body. Two sample assembly designs were used as depicted in Fig. 1(b). In the Type-I assembly, the Cu foil sample was sandwiched between two sapphire ( $\text{Al}_2\text{O}_3$ ) anvils that are excellent electrical insulators at high  $P$ - $T$  conditions [56]. The sapphire anvils were 25–30 mm in diameter and 2–3 mm in thickness. In the Type-II assembly, the Cu foil sample was sandwiched between

two 50- $\mu\text{m}$ -thick mica sheets and then clamped by two Cu anvils.

The skin depth ( $\delta$ ) is an important consideration for resistivity measurements under shock compression, which could be estimated by the formula [85]:

$$\delta = \sqrt{\frac{2\rho}{\omega\mu}} \sqrt{\sqrt{1 + (\rho\omega\epsilon)^2} + \rho\omega\epsilon}, \quad (2)$$

where  $\mu$  is the magnetic permeability ( $1.256 \times 10^{-6}$  H/m for Cu),  $\epsilon$  is the permittivity ( $8.854 \times 10^{-12}$  F/m for Cu [85]), and  $\omega$  is the angular frequency calculated as

$$\omega = 2\pi f, \quad (3)$$

where  $f$  is the current frequency. Equations (2) and (3) indicate that the skin depth decreases with increasing current frequency (Fig. S3 in the Supplemental Material [93]). Taking the duration from discharge initiation to peak current as

TABLE I. Impact conditions and results for the resistivity measurements of Cu under shock loading.  $w$  is the measured impact velocity of the flyer, and its uncertainty is  $\sim 0.5\%$ .  $\Delta T$  is the temperature rise caused by the current before the shock wave reaches the sample. The pressure ( $P$ ) and compression ratio ( $\eta$ ) in the shock-compressed sample are determined by the impedance matching method, and their uncertainties are estimated by the methods for error analysis in previous shock compression studies [101]. The temperature ( $T$ ) in the shock-compressed sample is estimated from the Hugoniot  $P$ - $T$  diagrams of  $\text{Al}_2\text{O}_3$  and Cu (Fig. S5 in the Supplemental Material [93]), and its uncertainty is estimated to be 12–15%.  $R_{S0}$  is the initial resistance of the sample, and its uncertainty is estimated to be  $<0.5\%$ .  $U_H$  and  $U_1$  denote the voltage across the sample in the shock compression and initial states, respectively, and the uncertainty in  $U_H/U_1$  can be estimated from the measured voltage profiles.  $\rho$ ,  $\sigma$ , and  $\kappa$  are the electrical resistivity, electrical conductivity, and thermal conductivity of Cu in the shock compression state, respectively, and their uncertainties are estimated from the errors in Hugoniot EoS,  $U_H/U_1$ , and the initial resistivity by using error propagation. Values in parentheses are uncertainties given at  $2\sigma$  levels.

| Shot No. | Sample assembly | Flyer/baseplate | $w$ (km/s) | $\Delta T$ (K) | $P$ (GPa)  | $T$ (K)   | $\eta$    | $R_{S0}$ (m $\Omega$ ) | $U_H/U_1$  | $\rho$ ( $\mu\Omega$ cm) | $\sigma$ ( $\mu\Omega$ dm) $^{-1}$ | $\kappa$ [W/(mK)] |
|----------|-----------------|-----------------|------------|----------------|------------|-----------|-----------|------------------------|------------|--------------------------|------------------------------------|-------------------|
| E1       | Type II         | Cu/Cu           | 2.360(12)  | 18(4)          | 59.9(0.6)  | 880(106)  | 0.793(24) | 21.15                  | 1.636(60)  | 2.40(17)                 | 4.16(29)                           | 556(77)           |
| E2       | Type I          |                 | 2.817(14)  | 15(3)          | 64.5(0.7)  | 800(120)  | 0.785(24) | 21.08                  | 1.581(132) | 2.27(23)                 | 4.40(45)                           | 530(96)           |
| E3       | Type II         |                 | 3.042(15)  | 14(3)          | 84.3(0.8)  | 1380(166) | 0.755(23) | 20.92                  | 2.016(125) | 2.77(24)                 | 3.61(31)                           | 689(101)          |
| E4       | Type I          |                 | 3.476(17)  | 12(2)          | 83.7(0.8)  | 1000(150) | 0.756(23) | 21.19                  | 1.881(178) | 2.57(29)                 | 3.89(43)                           | 543(101)          |
| E5       | Type II         |                 | 3.489(18)  | 12(2)          | 101.9(1.0) | 1790(215) | 0.733(22) | 21.13                  | 2.264(175) | 3.00(29)                 | 3.33(32)                           | 779(120)          |
| E6       | Type I          |                 | 4.553(23)  | 9(2)           | 118.3(1.2) | 1700(255) | 0.717(22) | 21.08                  | 2.613(272) | 3.35(40)                 | 2.99(36)                           | 638(122)          |

a half cycle yields an upper bound frequency estimate of  $2.5 \times 10^5$  Hz for the quasidirect current from the DC pulse power supply. The skin depth of Cu is then estimated to be  $\sim 130$   $\mu\text{m}$ , substantially exceeding the 10  $\mu\text{m}$  foil thickness used in this study. Since the entire sample lies within the skin depth, electrical resistivity measurements would be minimally impacted in the following experiments. Thus, skin depth corrections in data processing are unnecessary [85].

Prior to shock experiments, the initial electrical resistance ( $R_{S0}$ ) of the sample was measured using the DC source (Keithley 6221) and nanovoltmeter (Keithley 2182A) (Fig. S4 in the Supplemental Material [93]). The measured  $R_{S0}$  ranged from 20.92 to 21.19 m $\Omega$  (Table I), agreeing well with the ideal value of  $\sim 20.70$  m $\Omega$  calculated by

$$R = \rho \frac{l}{S}, \quad (4)$$

where  $R$  is the electrical resistance;  $l$  and  $S$  are the length and cross-sectional area of the sample, approximating  $1.2 \times 10^{-2}$  m and  $1 \times 10^{-8}$  m $^2$  under ambient conditions, respectively. To obtain input current and voltage profiles across the sample under ambient conditions, the power supply was manually triggered using identical settings as in shock experiments.

Six shots were performed with impact velocities spanning 2.36–4.55 km/s to measure the electrical resistivity of Cu. The experimental conditions including shock pressures, shock temperatures, and measured resistivities are listed in Table I. For the Type-I assembly, the impedance mismatch between Cu and  $\text{Al}_2\text{O}_3$  results in the Cu sample equilibrating to the Hugoniot state of the  $\text{Al}_2\text{O}_3$  anvil. For Type II, the thick Cu anvils and thin mica imply that the sample achieves an equilibrium state approximating the Hugoniot of the Cu anvil. Thus, the pressure in the shocked Cu sample was determined via the impedance matching method and the known Hugoniot relations for  $\text{Al}_2\text{O}_3$  [100] and Cu [101,102]. The shock-elevated temperature was estimated from the Hugoniot  $P$ - $T$  diagrams of  $\text{Al}_2\text{O}_3$  [103–105] and Cu [106–112] (Fig. S5 in the Supplemental Material [93]).

### C. FPMD simulations for electrical and thermal conductivity of Cu

Based on the Kubo-Greenwood (K-G) method [113–115], we performed first-principles calculations to investigate the electrical resistivity and electronic thermal conductivity of pure Cu under high  $P$ - $T$  conditions spanning 60–122 GPa and 1000–4000 K. To extend the  $P$ - $T$  conditions beyond the shock compression measurements, the deep potential molecular dynamics (DPMD) approach was employed [116]. The deep potential (DP) technique is a well-developed approach for learning first-principles data via deep neural networks, enabling the prediction of the potential energy and force of each atom [116–118].

High-quality training data were prepared via FPMD simulations using the plane-wave code VASP [119], which utilizes the projector augmented-wave (PAW) method to model ion-electron interactions [120,121]. The PAW\_PBEsol pseudopotential [122] with a  $3d^{10}4s^1$  valence configuration for Cu was implemented within an isothermal-isobaric ensemble (NPT) coupled with a Langevin thermostat [123]. Utilizing a cutoff energy of 400 eV and supercells comprising 256 atoms, convergence was achieved through  $\Gamma$ -point sampling. The lattice parameter of face-centered cubic (fcc) Cu was predicted to be 3.2868 Å using 256-atom cells at 84 GPa and 1350 K, which is overall consistent with the measurements (3.2886 Å) by shock wave experiments [101,102]. Our training dataset includes 28 000 configurations of fcc Cu derived from FPMD simulations under pressures of 60, 84, 102, and 122 GPa and temperatures of 1000, 2000, 3000, and 4000 K, respectively. The DeepMD-kit package [116] was then utilized to determine the machine learning potential (MLP) with a descriptor type of se\_e2\_a. The embedding network, comprising three hidden layers with 32, 64, and 128 nodes, was used to parameterize the descriptor. The fitting network, consisting of three layers with 240 nodes each, utilized a radius cutoff of 4 Å, employing conventional loss function parameters. The training process, spanning 400 000 steps, yielded root-mean-square errors of 0.88 meV/atom, 40 meV/Å, and 30 meV/atom for



energies, forces, and virial stresses, respectively. As shown in Fig. S6 in the Supplemental Material [93], the energies and forces predicted by MLP match perfectly with DFT.

The DP approach [124] was employed to compress the MLP. With a modified LAMMPS package [117,125], we ran the DPMD simulation with cells containing 256 atoms. As shown in Fig. S7 in the Supplemental Material [93], the volumes of the simulated unit cells agree well with the shock compression data [101,102]. The effect of size ranging from 256 to 1950 atoms on the unit cell volume was investigated, showing a marginal difference of merely 0.8%. The radial distribution function, computed for fcc Cu at 84 GPa and 1000 K using DPMD within a canonical ensemble, demonstrates strong concordance with the FPMD results (Fig. S8 in the Supplemental Material [93]), thereby validating the precision of our MPL.

Supercells comprising 108 Cu atoms were constructed with the EoS predicted by DPMD at the targeted  $P$ - $T$  conditions. Subsequent FPMD simulations, utilizing a canonical ensemble (NVT) with the Nosé-Hoover thermostat [126,127], facilitated the acquisition of ionic configurations. The Brillouin zone was sampled by the  $\Gamma$  point, and the electronic states were occupied according to Fermi-Dirac statistics. The cutoff energy and pseudopotential file were 400 eV and PAW\_PBE type, respectively. The simulation continued running for 10 ps after an initial 1 ps for equilibration. Snapshots of nuclear positions were extracted every 500 MD steps during the final 5 ps. A modified KG4VASP package [128] was used to compute the electrical resistivity and thermal conductivity of Cu through the K-G method. Dirac  $\delta$  functions were approximated as one Gaussian function with a spreading of 20 meV. The transport properties at zero frequency were obtained by linear extrapolation. Results were averaged over snapshots with the standard deviation taken as uncertainty. In comparison with the 256-atom cell, a 108-atom supercell equipped with a dense  $5 \times 5 \times 5$   $k$ -points grid was adequate for computing the electrical conductivity of Cu at the  $P$ - $T$  conditions investigated in this study, with the difference being  $<5\%$  (Fig. S9 in the Supplemental Material [93]). The thermal conductivities exhibit nearly identical values between the 108- and 256-atom cells, indicating a minor impact stemming from cell size. Additionally, we validated the electrical resistivity of Cu at 0 GPa and 1350 K, yielding a value of 22.9(6)  $\mu\Omega$  cm (Fig. S10 in the Supplemental Material [93]), consistent with the FPMD result of  $\sim 23$   $\mu\Omega$  cm reported in Ref. [34].

### III. RESULTS AND DISCUSSION

#### A. Electrical resistivity of Cu at high pressure and room temperature

The electrical resistivity of Cu was measured up to a static pressure of 50 GPa in the DAC at room temperature (Fig. 2). Our results show that the resistivity of Cu gradually diminishes with increasing pressure, decreasing by  $\sim 45\%$  at 50 GPa. The smooth change in resistivity indicates that no electronic or structural phase transitions occur within the measured pressure range, consistent with previous studies [129,130]. For a metal at high pressures without phase transitions, the resistivity at room temperature (300 K) can

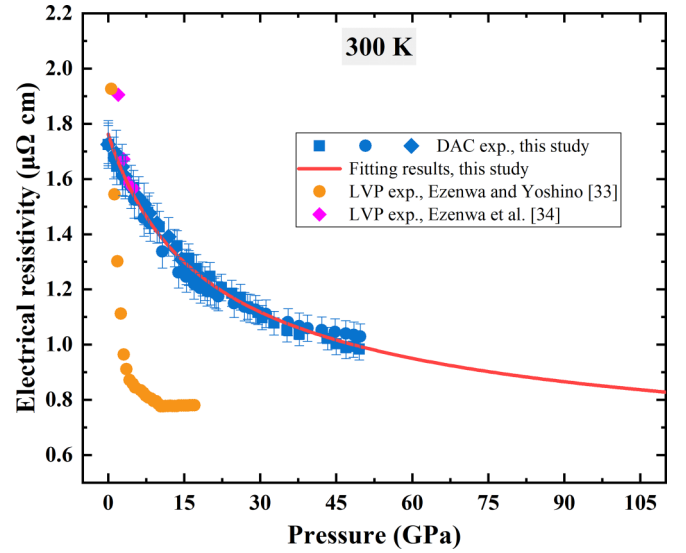


FIG. 2. Electrical resistivity of Cu as a function of pressure at room temperature (300 K) within a diamond-anvil cell (DAC). The blue rectangles, circles, and diamonds represent distinct runs conducted in this study; the red curve depicts a fitted model to our collected data; the orange circles and carmine diamonds are measurements performed by Ezenwa and Yoshino [33] and Ezenwa *et al.* [34] using the large-volume press (LVP) with different assemblies, respectively.

be fitted by [45]

$$\rho(V, 300 \text{ K}) = F_1 \times \left( F_2 - \frac{V}{V_0} \right)^{F_3}, \quad (5)$$

where  $F_1$ ,  $F_2$ , and  $F_3$  are fitting parameters. Our data are well fitted by Eq. (5) with  $F_1 = 4.58(25)$   $\mu\Omega$  cm,  $F_2 = 1.19(7)$ , and  $F_3 = -0.81(13)$  (Fig. 2).

The measured resistivities in our DAC experiments are overall consistent with the results up to  $\sim 5$  GPa in the early LVP experiments conducted by Ezenwa *et al.* [34]. However, a noticeable deviation is observed in comparison with results obtained by Ezenwa and Yoshino [33] at pressures up to  $\sim 16$  GPa in the LVP with a different assembly. This divergence may arise from disparities in experimental methodologies and sample geometries. Specifically, the use of varied assembly configurations in the LVP experiments could lead to different responses and may be susceptible to errors in determining the geometry of *ex situ* recovered samples [33]. Additionally, variations in pressure calibration, measurement techniques, sample environment, and the scale of samples between the LVP and our DAC measurements could contribute to the observed discrepancies in resistivities [6]. These factors highlight the sensitivity of resistivity measurements to specific experimental setup, particularly under high  $P$ - $T$  scenarios.

#### B. Normalized resistance of Cu in dynamic compression measurements

Typical voltage and current profiles for resistivity measurements of Cu under shock compression are shown in Fig. 3(a).

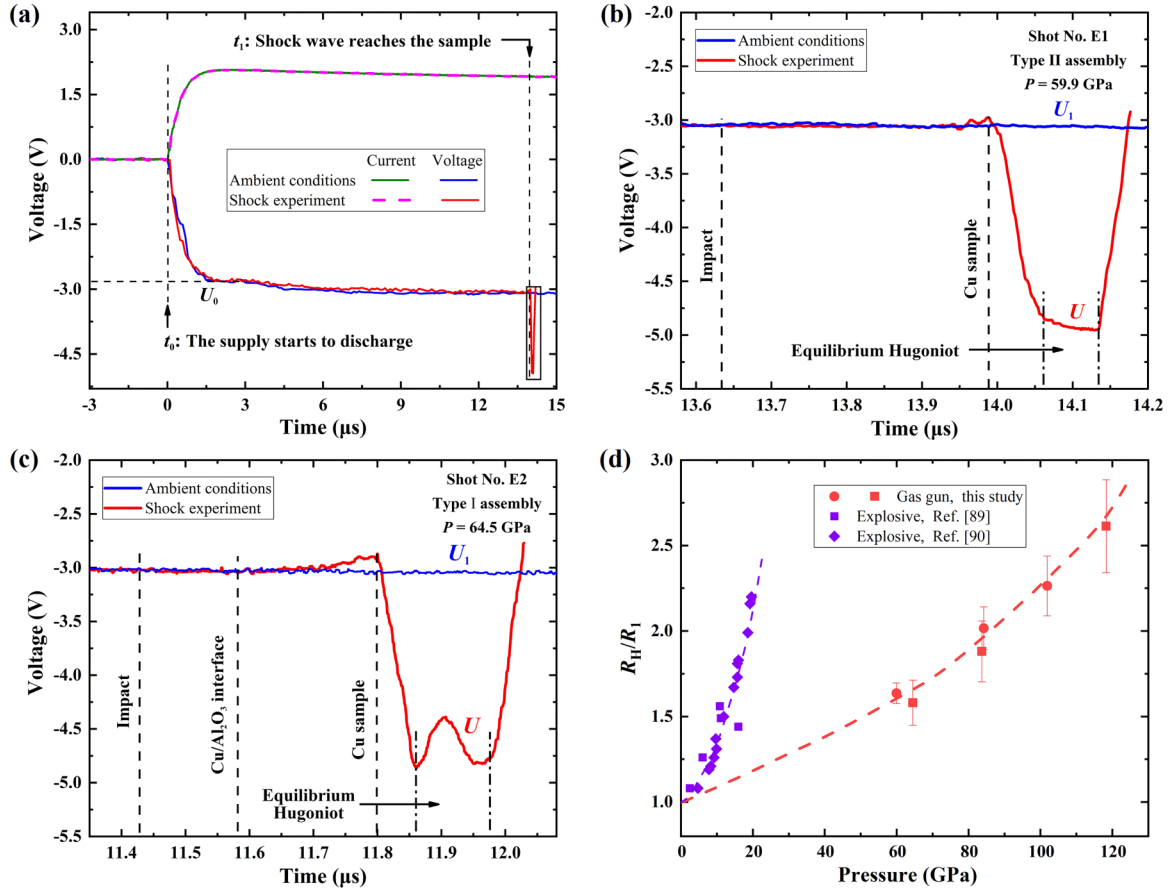


FIG. 3. Typical voltage profiles and electrical resistivity of Cu under shock compression. (a) Typical voltage and current (Rogowski coil) profiles in shot No. E1 obtained by using the Type-II sample assembly. (b) Enlargement of the boxed region in (a), highlighting the sharp voltage change during shock loading. (c) The voltage profile in shot No. E2 obtained by using the Type-I sample assembly. The vertical black dashed lines are presented to show the experimental timings of the shock wave front. (d) Normalized resistance ( $R_H/R_1$ ) of Cu under shock compression. The red rectangles and circles are the results of our dynamic measurements using Type-I and II sample assemblies, respectively, in a two-stage light-gas gun; the violet rectangles [89] and diamonds [90] are the results of previous measurements using the noncontact method and the four-probe method, respectively, in the high explosive shock apparatus. The red dashed line is a guide to the eye, showing the trend of the normalized resistance in this study.

The DC pulse power supply was triggered at  $t_0 = 0$  μs. The current and voltage rapidly increased in 0–2 μs and then remained essentially constant. The voltage and current profiles overlapped between the test run at ambient conditions and the shock experiments until the shock wave reached the sample at  $t_1 = \sim 14$  μs. The detailed voltage changes under shock loading for the Type-II and I sample assemblies are shown in Figs. 3(b) and 3(c), respectively. The voltage increased quickly and then fluctuated within a small range, showing that an equilibrium Hugoniot state lasted for  $\sim 70$ –100 ns. Similar fluctuations were observed by Crum *et al.* [85] using the Type-I assembly with thin tin (Sn) film samples. Shock temperature measurements show that tiny gaps ( $\sim 1$  μm) between the sample and window dramatically affect results [131–133]. Thus, the fluctuations likely arise from gaps between the sample and the Al<sub>2</sub>O<sub>3</sub> anvils. Achieving near-ideal contact is challenging due to the high sapphire hardness. To minimize gap effects, we employed soft mica as an insulating layer placed between the sample and the Cu anvils in the Type-II sample assembly. This significantly reduced the magnitude of the voltage fluctuations [Figs. 3(b) and 3(c)].

The input current was the same during test runs at ambient conditions and shock experiments (Fig. 3). Based on Ohm's law, the voltage change directly relates to the resistance change. Thus, the normalized resistance ( $R_H/R_1$ ), defined as the ratio of the resistance under shock loading to that before, is obtained from the measured voltage profile as

$$\frac{U_H}{U_1} = \frac{I_H R_H}{I_1 R_1} = \frac{R_H}{R_1}, \quad (6)$$

where  $U$  and  $I$  are the voltage across and current through the sample, respectively; subscripts  $H$  and  $1$  denote the equilibrium Hugoniot state and the initial state when the shock wave arrives, respectively. Overall, the measured normalized resistance increased with increasing shock pressure [Fig. 3(d)]. For comparison, we also show previous dynamic measurements at lower pressures using noncontact [89] and four-probe [90] methods in Fig. 3(d), which have a steeper increase. Extrapolating our data suggests significantly lower resistivities than those previous work [89,90]. For example, they obtained a normalized resistance of  $\sim 2.2$  at a shock  $P$ - $T$  condition of 20 GPa and  $\sim 460$  K [89,90], whereas the temperature rise of

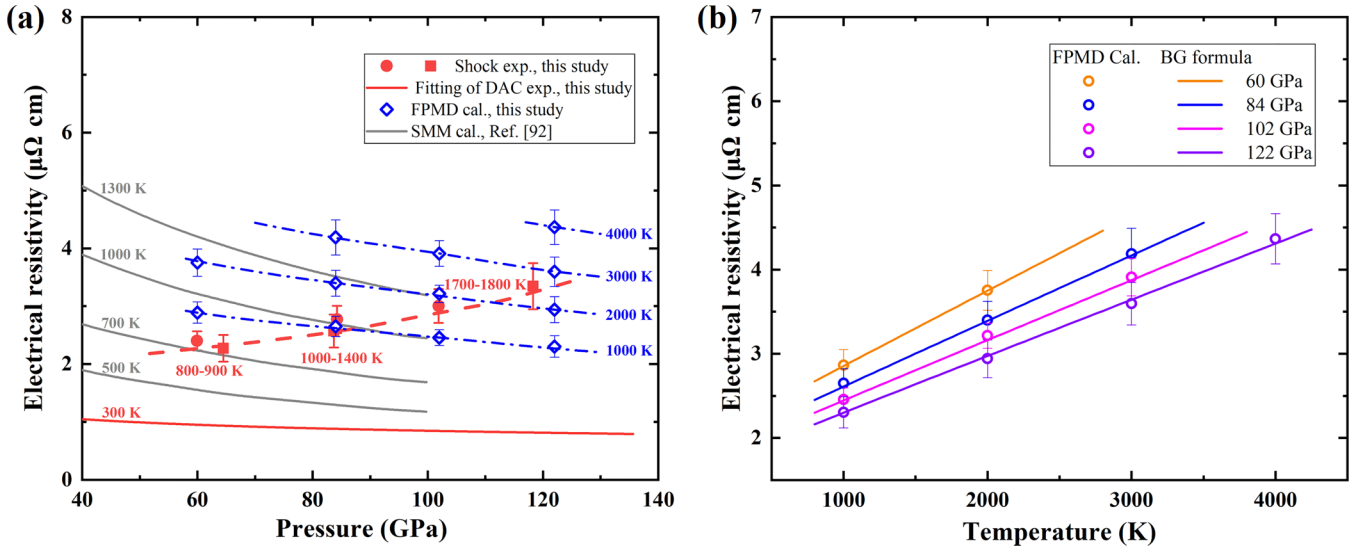


FIG. 4. Electrical resistivity of solid Cu at high  $P$ - $T$ . (a) Pressure-dependent electrical resistivity of solid Cu at high temperatures. The red rectangles and circles are our measured resistivity of Cu using Type-I and II sample assemblies, respectively; the solid red line is the fitting results of our diamond-anvil cell (DAC) measurements at 300 K; the blue diamonds are the results of our first-principles molecular dynamics (FPMD) simulations; the gray curves [92] are the results of statistical moment method (SMM) calculations. The red dashed and blue dotted dashed lines are guides to the eye, showing the trend of our measured and simulated electrical resistivity, respectively; the numbers of the same color next to the lines and legends represent the temperature. (b) Temperature-dependent electrical resistivity of solid Cu at high pressures determined by FPMD simulations. The orange, blue, carmine, and violet circles are the calculated results at 60, 84, 102, and 122 GPa, respectively, and the corresponding solid lines are the resistivity of face-centered cubic (fcc) Cu fitted by the Bloch-Grüneisen formula.

$\sim 160$  K would only increase the resistivity of Cu by a factor of  $\sim 1.6$  [87]. This indicates previous dynamic measurements substantially overestimated the resistivity.

In the noncontact method, the attenuation of eddy currents of Cu under shock compression in a finite-sized foil disk sample was measured to derive the resistivity [89]. However, their induction sensor signals changed slightly under shock loading. Additionally, the procedure for processing the low signal-to-noise data is rather complex, further inducing uncertainty. Although the four-probe method has been used in some previous experiments [90], plate movement between the explosive and sample perturbed the magnetic field, reducing the voltage [134] and abnormally increasing the normalized resistance. Here, the Cu baseplate used in this study could avoid such flyer-induced perturbations.

### C. Electrical and thermal conductivity of Cu under high pressure and temperature conditions

Combining Eqs. (4) and (6) gives the electrical resistivity ( $\rho_H$ ) and conductivity ( $\sigma_H$ ) in the equilibrium Hugoniot state:

$$\rho_H = \frac{1}{\sigma_H} = \eta \rho_1 \frac{U_H}{U_1}, \quad (7)$$

where  $\eta$  is the compression ratio and  $\rho_1$  is the electrical resistivity at  $t_1$ . Here,  $\eta$  was estimated via the Rankine-Hugoniot equations [101]:

$$\eta = \frac{d_0}{d_H} = \frac{S_H}{S_0}, \quad (8)$$

where  $d$  is the density. Here,  $\rho_1$  depends on the initial temperature rise ( $\Delta T$ ) from Joule heating before shock arrival, estimated as

$$\Delta T = \frac{Q}{mc}, \quad (9)$$

where  $m$  and  $c$  are the mass and heat capacity of the Cu sample, respectively, with  $c = 0.385 \times 10^3 \text{ J/(kg K)}$  [135];  $Q$  is the heat generated:

$$Q = \frac{\left(\frac{U_0 + U_1}{2}\right)^2}{R_0} (t_1 - t_0), \quad (10)$$

and  $\Delta T$  ranged from 9 to 18 K (Table I). With known  $\rho_1$  [87], the measured normalized resistance gives  $\rho_H$  in the  $P$ - $T$  range of 60–118 GPa and 800–1800 K [Table I, Fig. 4(a)]. Here,  $\rho_H$  increases overall from 2.27–2.40  $\mu\Omega \text{ cm}$  at 60–65 GPa and 800–900 K to 3.00–3.35  $\mu\Omega \text{ cm}$  at 100–120 GPa and 1700–1800 K. The Type-I assembly gave slightly lower  $\rho_H$  than the Type II at fixed pressures, likely due to different shock-elevated temperatures in the anvils.

The resistivity obtained from our shock experiments at high  $P$ - $T$  is significantly higher than that extrapolated from our DAC experiments due to the shock-elevated temperature. We performed FPMD simulations to elucidate the separate effects of pressure and temperature on the transport properties of fcc Cu in the  $P$ - $T$  range of 60–122 GPa and 1000–4000 K. As expected, the simulated resistivity exhibits a pressure-induced decrease and a temperature-induced increase (Fig. 4). Overall, the FPMD simulations agree well with our dynamic measurements, supporting our methodology for probing ultra-high  $P$ - $T$  resistivity. We compared our resistivity data at high

TABLE II. Parameters for the Bloch-Grüneisen formula in the electrical resistivity of Cu under high  $P$ - $T$  conditions.

| Pressure<br>(GPa) | $V/V_0$ | $\theta_R(V)$<br>(K) | $\rho_{\text{res}}(V)$<br>( $\mu\Omega$ cm) | $\alpha_{\text{el-ph}}(V)$<br>( $\mu\Omega$ cm) | $n$ |
|-------------------|---------|----------------------|---|---|-----|
| 60                | 0.783   | 532                  | 1.98(20)                                    | 1.89(23)  | 5   |
| 84                | 0.738   | 584                  | 1.85(25)                                    | 1.81(28)  | 5   |
| 102               | 0.713   | 616                  | 1.75(21)                                    | 1.76(25)  | 5   |
| 122               | 0.689   | 650                  | 1.65(27)                                    | 1.73(32)  | 5   |

$P$ - $T$  with the SMM predictions [Fig. 4(a)] [92]. Our data are generally consistent with the SMM predictions at 60–84 GPa and 800–1000 K. However, at higher  $P$ - $T$  conditions, SMM may underestimate resistivity, possibly due to underestimation of the Debye temperature and/or overestimation of the cell volume.

Our results show that the resistivity of fcc Cu increases linearly with increasing temperature at high pressures, which can be described by the Bloch-Grüneisen formula:

$$\begin{aligned}\rho(V, T) &= \rho_{\text{res}}(V) + \rho_{\text{BG}}(V, T) \\ &= \rho_{\text{res}}(V) + \alpha_{\text{el-ph}}(V) \left( \frac{T}{\theta_D(V)} \right)^n \\ &\quad \times \int_0^{\theta_R(V)/T} \left[ \frac{x^n}{(e^x - 1)(1 - e^{-x})} \right] dx, \quad (11)\end{aligned}$$

where  $\rho_{\text{res}}(V)$  represents the residual resistivity arising primarily from the defect scattering, intrinsically independent of temperature; the pressure-dependent and temperature-dependent component  $\rho_{\text{BG}}(V, T)$  arises from electron-phonon interactions;  $\alpha_{\text{el-ph}}(V)$  denotes a material constant; the constant  $n$  is typically an integer number (2, 3, and 5), which can be taken as 5 for Cu given its reasonable mean free path [136];  $\theta_D(V)$  corresponds to the Debye temperature, which varies solely with volume per the Debye model:

$$\gamma = -\frac{d \ln [\theta_D(V)]}{d \ln V}, \quad (12)$$

where the Grüneisen parameter  $\gamma$  and the volume  $V$  of Cu at high pressures are available from the literature [96,137]. The Debye temperature of Cu under ambient conditions is 343 K [33]. Solving this equation yielded the  $\theta_D(V)$  of Cu at high pressures, which increases with increasing pressure from  $\sim 532$  K at 60 GPa to  $\sim 650$  K at 122 GPa (Fig. S11 in the Supplemental Material [93]).

The excellent fit of our data to the Bloch-Grüneisen formula confirms the electron-phonon scattering as the primary resistivity mechanism for fcc Cu at high  $P$ - $T$  [Fig. 4(b)]. The fitted parameters at each pressure are shown in Table II and Fig. S11 in the Supplemental Material [93]. Both  $\rho_{\text{res}}(V)$  and  $\alpha_{\text{el-ph}}(V)$  decrease with increasing pressure, showing that the temperature-dependent resistivity weakens at higher pressures. This indicates that elevated pressures reduce the impedance to free electron migration in Cu, consistent with other metals [3]. Notably, resistivity saturation in solid Cu was

not observed within our investigated  $P$ - $T$  range, implying that the mean free path of the electrons is not yet comparable with their wavelength [138].

The electrical conductivity also provides insight into the thermal conductivity via the Wiedemann-Franz law [139] (Fig. S12(a) and Text S1 in the Supplemental Material [93]). However, our computed thermal conductivity exceeds the results converted from experimental resistivity, indicating the breakdown of the ideal Wiedemann-Franz law for Cu under high  $P$ - $T$  conditions. In this regime, the calculated Lorentz number ( $L$ ) of fcc Cu at high  $P$ - $T$  is higher than the ideal Sommerfeld value ( $L_0 = 2.445 \times 10^{-8} \text{ W}\Omega/\text{K}^2$ ) [140,141] (Fig. S12(b) in the Supplemental Material [93]), like other fcc structural transition metals such as platinum (Pt) [21]. The deviation of the Lorentz number may be related to the electronic specific heat [142]. At high temperatures, the electronic specific heat for copper, gold, and iron exhibits a faster increase than the Sommerfeld value with rising temperature, resulting in a higher Lorentz number than the ideal Sommerfeld value [143]. This elevated Lorentz number suggests enhanced electronic contributions to thermal conductivity, emphasizing the significance of considering the dynamic nature of electron-phonon interactions at extreme conditions.

#### IV. CONCLUSIONS

In summary, we investigated the electrical and thermal conductivity of Cu up to  $\sim 120$  GPa and 4000 K by both *in situ* experiments and FPMD simulations. The results obtained through both avenues exhibit excellent agreement. Specifically, we observed a gradual decrease in the electrical resistivity of Cu with increasing pressure and a corresponding increase with rising temperature. The relationship between electrical resistivity and temperature for fcc Cu overall follows the Bloch-Grüneisen formula, confirming electron-phonon scattering as its predominant resistivity mechanism. Notably, the Lorenz number of fcc Cu at high  $P$ - $T$  exceeds the ideal Sommerfeld value ( $2.445 \times 10^{-8} \text{ W}\Omega/\text{K}^2$ ), indicating the breakdown of the ideal Wiedemann-Franz law under extreme pressure-temperature conditions. In conclusion, our complementary studies provide insight into the electrical and thermal transport properties of transition metals under extreme  $P$ - $T$  conditions.

#### ACKNOWLEDGMENTS

We acknowledge Shangchun Shi, Jinde Liu, Yuqian Huang, Xiaohong Li, and Qiming Wang for their assistance in shock experiments and data analysis. This work was supported by the National Key Laboratory of Shock Wave and Detonation Physics (Grant No. 2022JCJQLB05701), the Sichuan Science and Technology Program (Grant No. 2023NSFSC1910), the China Postdoctoral Science Foundation (Grant No. GZC20231765), and the Institutional Research Fund from Sichuan University (Grant No. 2022SCUNL102).

[1] L. Deng, C. Seagle, Y. Fei, and A. Shahar, High pressure and temperature electrical resistivity of iron and

implications for planetary cores, *Geophys. Res. Lett.* **40**, 33 (2013).



- [2] Z. Konôpková, R. S. McWilliams, N. Gómez-Pérez, and A. F. Goncharov, Direct measurement of thermal conductivity in solid iron at planetary core conditions, *Nature (London)* **534**, 99 (2016).
- [3] K. Ohta, Y. Kuwayama, K. Hirose, K. Shimizu, and Y. Ohishi, Experimental determination of the electrical resistivity of iron at Earth's core conditions, *Nature (London)* **534**, 95 (2016).
- [4] S. Park, H. Lee, J. Ryu, K.-J. Chung, Y. S. Hwang, K. Lee, and D.-K. Kim, Measurement on the electrical conductivity of copper along the binodal curve in warm dense regime, *Appl. Phys. Lett.* **119**, 174102 (2021).
- [5] Y. Zhang, M. Hou, G. Liu, C. Zhang, V. B. Prakapenka, E. Greenberg, Y. Fei, R. E. Cohen, and J. F. Lin, Reconciliation of experiments and theory on transport properties of iron and the geodynamo, *Phys. Rev. Lett.* **125**, 078501 (2020).
- [6] M. Berrada and R. A. Secco, Review of electrical resistivity measurements and calculations of Fe and Fe-alloys relating to planetary cores, *Front. Earth Sci.* **9**, 732289 (2021).
- [7] S. D. Gilev, Measurement of electrical conductivity of condensed substances in shock waves (Review), *Combust. Explos. Shock Waves* **47**, 375 (2011).
- [8] M. Pozzo, C. Davies, D. Gubbins, and D. Alfè, Thermal and electrical conductivity of solid iron and iron-silicon mixtures at Earth's core conditions, *Earth Planet. Sci. Lett.* **393**, 159 (2014).
- [9] X. Sha and R. E. Cohen, First-principles studies of electrical resistivity of iron under pressure, *J. Phys.: Condens. Matter* **23**, 075401 (2011).
- [10] F. D. Stacey and D. E. Loper, A revised estimate of the conductivity of iron alloy at high pressure and implications for the core energy balance, *Phys. Earth Planet. Inter.* **161**, 13 (2007).
- [11] F. D. Stacey and O. L. Anderson, Electrical and thermal conductivities of Fe–Ni–Si alloy under core conditions, *Phys. Earth Planet. Inter.* **124**, 153 (2001).
- [12] M. Pozzo, C. Davies, D. Gubbins, and D. Alfè, Thermal and electrical conductivity of iron at Earth's core conditions, *Nature (London)* **485**, 355 (2012).
- [13] X. Zhang, S. Li, A. Wang, and H. Bao, Pressure-dependent thermal conductivity in Al, W, and Pt: Role of electrons and phonons, *Phys. Rev. B* **106**, 094313 (2022).
- [14] S.-Y. Yue and M. Hu, Insight of the thermal conductivity of  $\epsilon$ -iron at Earth's core conditions from the newly developed direct *ab initio* methodology, *J. Appl. Phys.* **125**, 045102 (2019).
- [15] K. Ramakrishna, M. Lokamani, A. Baczewski, J. Vorberger, and A. Cangi, Electrical conductivity of iron in Earth's core from microscopic Ohm's law, *Phys. Rev. B* **107**, 115131 (2023).
- [16] F. Wagle and G. Steinle-Neumann, Electrical resistivity discontinuity of iron along the melting curve, *Geophys. J. Int.* **213**, 237 (2018).
- [17] F. Wagle, G. Steinle-Neumann, and N. de Koker, Saturation and negative temperature coefficient of electrical resistivity in liquid iron-sulfur alloys at high densities from first-principles calculations, *Phys. Rev. B* **97**, 094307 (2018).
- [18] J. Xu, P. Zhang, K. Haule, J. Minar, S. Wimmer, H. Ebert, and R. E. Cohen, Thermal conductivity and electrical resistivity of solid iron at Earth's core conditions from first principles, *Phys. Rev. Lett.* **121**, 096601 (2018).
- [19] F. Soubiran and B. Militzer, Electrical conductivity and magnetic dynamos in magma oceans of super-earths, *Nat. Commun.* **9**, 3883 (2018).
- [20] E. Holmström, L. Stixrude, R. Scipioni, and A. S. Foster, Electronic conductivity of solid and liquid (Mg, Fe)O computed from first principles, *Earth Planet. Sci. Lett.* **490**, 11 (2018).
- [21] H. Gomi and T. Yoshino, Resistivity, Seebeck coefficient, and thermal conductivity of platinum at high pressure and temperature, *Phys. Rev. B* **100**, 214302 (2019).
- [22] N. A. Smirnov, *Ab initio* calculations for the transport properties of metals within Boltzmann transport theory: From equilibrium to nonequilibrium heating regime, *Phys. Rev. B* **106**, 024109 (2022).
- [23] B. Xu, M. Di Gennaro, and M. J. Verstraete, Thermoelectric properties of elemental metals from first-principles electron-phonon coupling, *Phys. Rev. B* **102**, 155128 (2020).
- [24] V. Vlček, N. de Koker, and G. Steinle-Neumann, Electrical and thermal conductivity of Al liquid at high pressures and temperatures from *ab initio* computations, *Phys. Rev. B* **85**, 184201 (2012).
- [25] N. De Koker, G. Steinle-Neumann, and V. Vlček, Electrical resistivity and thermal conductivity of liquid Fe alloys at high  $P$  and  $T$ , and heat flux in Earth's core, *Proc. Natl. Acad. Sci. USA* **109**, 4070 (2012).
- [26] I. C. Ezenwa and R. A. Secco, Invariant electrical resistivity of Co along the melting boundary, *Earth Planet. Sci. Lett.* **474**, 120 (2017).
- [27] I. C. Ezenwa and R. A. Secco, Electronic transition in solid Nb at high pressure and temperature, *J. Appl. Phys.* **121**, 225903 (2017).
- [28] I. C. Ezenwa and R. A. Secco, Constant electrical resistivity of Zn along the melting boundary up to 5 GPa, *High Pressure Res.* **37**, 319 (2017).
- [29] I. C. Ezenwa and T. Yoshino, Electrical resistivity of solid and liquid Pt: Insight into electrical resistivity of  $\epsilon$ -Fe, *Earth Planet. Sci. Lett.* **544**, 116380 (2020).
- [30] I. C. Ezenwa and R. A. Secco, Fe melting transition electrical resistivity thermal conductivity heat flow at the inner core boundaries of Mercury and Ganymede, *Crystals* **9**, 359 (2019).
- [31] R. E. Silber, R. A. Secco, W. Yong, and J. A. H. Littleton, Electrical resistivity of liquid Fe to 12 GPa: Implications for heat flow in cores of terrestrial bodies, *Sci. Rep.* **8**, 10758 (2018).
- [32] R. E. Silber, R. A. Secco, W. Yong, and J. A. H. Littleton, Heat flow in Earth's core from invariant electrical resistivity of Fe-Si on the melting boundary to 9 GPa: Do light elements matter? *J. Geophys. Res.: Solid Earth* **124**, 5521 (2019).
- [33] I. C. Ezenwa and T. Yoshino, Electrical resistivity of Cu and Au at high pressure above 5 GPa: Implications for the constant electrical resistivity theory along the melting curve of the simple metals, *Materials* **14**, 5476 (2021).
- [34] I. C. Ezenwa, R. A. Secco, W. Yong, M. Pozzo, and D. Alfè, Electrical resistivity of solid and liquid Cu up to 5 GPa: Decrease along the melting boundary, *J. Phys. Chem. Solids* **110**, 386 (2017).
- [35] J. A. H. Littleton, R. A. Secco, and W. Yong, Decreasing electrical resistivity of silver along the melting boundary up to 5 GPa, *High Pressure Res.* **38**, 99 (2018).
- [36] M. Berrada, R. A. Secco, and W. Yong, Decreasing electrical resistivity of gold along the melting boundary up to 5 GPa, *High Pressure Res.* **38**, 367 (2018).

- [37] R. C. Liebermann, Multi-anvil, high pressure apparatus: A half-century of development and progress, *High Pressure Res.* **31**, 493 (2011).
- [38] Y. Yin, L. Wang, S. Zhai, and Y. Fei, Electrical resistivity of Fe and Fe-3 wt %P at 5 GPa with implications for the Moon's core conductivity and dynamo, *J. Geophys. Res.: Planets* **127**, e2021JE007116 (2022).
- [39] A. Dewaele, P. Loubeyre, F. Occelli, O. Marie, and M. Mezouar, Toroidal diamond anvil cell for detailed measurements under extreme static pressures, *Nat. Commun.* **9**, 2913 (2018).
- [40] N. Dubrovinskaia, L. Dubrovinsky, N. A. Solopova, A. Abakumov, S. Turner, M. Hanfland, E. Bykova, M. Bykov, C. Prescher, V. B. Prakapenka *et al.*, Terapascal static pressure generation with ultrahigh yield strength nanodiamond, *Sci. Adv.* **2**, e1600341 (2016).
- [41] L. Dubrovinsky, N. Dubrovinskaia, V. B. Prakapenka, and A. M. Abakumov, Implementation of micro-ball nanodiamond anvils for high-pressure studies above 6 Mbar, *Nat. Commun.* **3**, 1163 (2012).
- [42] P. Parisiades, A review of the melting curves of transition metals at high pressures using static compression techniques, *Crystals* **11**, 416 (2021).
- [43] S. M. Arveson, B. Kiefer, J. Deng, Z. Liu, and K. K. M. Lee, Thermally induced coloration of KBr at high pressures, *Phys. Rev. B* **97**, 094103 (2018).
- [44] R. A. Fischer, E. Cottrell, E. Hauri, K. K. M. Lee, and M. Le Voyer, The carbon content of Earth and its core, *Proc. Natl. Acad. Sci. USA* **117**, 8743 (2020).
- [45] H. Gomi, K. Ohta, K. Hirose, S. Labrosse, R. Caracas, M. J. Verstraete, and J. W. Hernlund, The high conductivity of iron and thermal evolution of the Earth's core, *Phys. Earth Planet. Inter.* **224**, 88 (2013).
- [46] R. A. Secco, Thermal conductivity and Seebeck coefficient of Fe and Fe-Si alloys: Implications for variable Lorenz number, *Phys. Earth Planet. Inter.* **265**, 23 (2017).
- [47] K. M. Bulatov, A. N. Semenov, A. A. Bykov, A. S. Machikhin, K. D. Litasov, P. V. Zinin, and S. V. Rashchenko, Measurement of thermal conductivity in laser-heated diamond anvil cell using radial temperature distribution, *High Pressure Res.* **40**, 315 (2020).
- [48] Y. Zhang, K. Luo, M. Hou, P. Driscoll, N. P. Salke, J. Minár, V. B. Prakapenka, E. Greenberg, R. J. Hemley, R. E. Cohen *et al.*, Thermal conductivity of Fe-Si alloys and thermal stratification in Earth's core, *Proc. Natl. Acad. Sci. USA* **119**, e2119001119 (2022).
- [49] Y. Zhang, M. Hou, P. Driscoll, N. P. Salke, J. Liu, E. Greenberg, V. B. Prakapenka, and J.-F. Lin, Transport properties of Fe-Ni-Si alloys at Earth's core conditions: Insight into the viability of thermal and compositional convection, *Earth Planet. Sci. Lett.* **553**, 116614 (2021).
- [50] I. C. Ezenwa and T. Yoshino, Martian core heat flux: Electrical resistivity and thermal conductivity of liquid Fe at Martian core  $P$ - $T$  conditions, *Icarus* **360**, 114367 (2021).
- [51] C. T. Seagle, E. Cottrell, Y. Fei, D. R. Hummer, and V. B. Prakapenka, Electrical and thermal transport properties of iron and iron-silicon alloy at high pressure, *Geophys. Res. Lett.* **40**, 5377 (2013).
- [52] N. Velisavljevic, K. M. MacMinn, Y. K. Vohra, and S. T. Weir, Electrical measurements on praseodymium metal to 179 GPa using designer diamond anvils, *Appl. Phys. Lett.* **84**, 927 (2004).
- [53] R. L. Reichlin, Measuring the electrical resistance of metals to 40 GPa in the diamond-anvil cell, *Rev. Sci. Instrum.* **54**, 1674 (1983).
- [54] A. Basu, M. R. Field, D. G. McCulloch, and R. Boehler, New measurement of melting and thermal conductivity of iron close to outer core conditions, *Geosci. Front.* **11**, 565 (2020).
- [55] M. Li, C. Gao, Y. Ma, D. Wang, Y. Li, and J. Liu, *In situ* electrical conductivity measurement of high-pressure molten  $(\text{Mg}_{0.875}, \text{Fe}_{0.125})_2\text{SiO}_4$ , *Appl. Phys. Lett.* **90**, 113507 (2007).
- [56] S. T. Weir, A. C. Mitchell, and W. J. Nellis, Electrical resistivity of single-crystal  $\text{Al}_2\text{O}_3$  shock-compressed in the pressure range 91–220 GPa (0.91–2.20 Mbar), *J. Appl. Phys.* **80**, 1522 (1996).
- [57] T. Mashimo, R. Chau, Y. Zhang, T. Kobayoshi, T. Sekine, K. Fukuoka, Y. Syono, M. Kodama, and W. J. Nellis, Transition to a virtually incompressible oxide phase at a shock pressure of 120 GPa (1.2 Mbar):  $\text{Gd}_3\text{Ga}_5\text{O}_{12}$ , *Phys. Rev. Lett.* **96**, 105504 (2006).
- [58] A. A. Golyshev and A. M. Molodets, Electrical resistivity of plastic insulation at megabar shock pressures, *Combust. Explos. Shock Waves* **49**, 219 (2013).
- [59] V. I. Tarzhanov, Y. N. Zhugin, and K. K. Krupnikov, Electrical conductivity of polytetrafluoroethylene under shock-wave loading and rarefaction, *J. Appl. Mech. Tech. Phys.* **38**, 826 (1997).
- [60] S. A. Bordzilovskii and S. M. Karakhanov, Electrical insulating properties of fluoroplastic interlayers under dynamic compression, *Combust. Explos. Shock Waves* **26**, 485 (1990).
- [61] S. A. Bordzilovskii and S. M. Karakhanov, Electric resistance of polytetrafluoroethylene under shock compression, *Combust. Explos. Shock Waves* **38**, 722 (2002).
- [62] T. Mashimo, K.-I. Kondo, A. Sawaoka, Y. Syono, H. Takei, and T. J. Ahrens, Electrical conductivity measurement of fayalite under shock compression up to 56 GPa, *J. Geophys. Res.: Solid Earth* **85**, 1876 (1980).
- [63] W. J. Nellis, The unusual magnetic fields of Uranus and Neptune, *Mod. Phys. Lett. B* **29**, 1430018 (2015).
- [64] R. Chau, S. Hamel, and W. J. Nellis, Chemical processes in the deep interior of Uranus, *Nat. Commun.* **2**, 203 (2011).
- [65] R. Chau, A. C. Mitchell, R. W. Minich, and W. J. Nellis, Electrical conductivity of water compressed dynamically to pressures of 70–180 GPa (0.7–1.8 Mbar), *J. Chem. Phys.* **114**, 1361 (2001).
- [66] P. M. Celliers, G. W. Collins, D. G. Hicks, M. Koenig, E. Henry, A. Benuzzi-Mounaix, D. Batani, D. K. Bradley, L. B. Da Silva, R. J. Wallace *et al.*, Electronic conduction in shock-compressed water, *Phys. Plasmas* **11**, L41 (2004).
- [67] P. Loubeyre, P. M. Celliers, D. G. Hicks, E. Henry, A. Dewaele, J. Pasley, J. Eggert, M. Koenig, F. Occelli, K. M. Lee *et al.*, Coupling static and dynamic compressions: First measurements in dense hydrogen, *High Pressure Res.* **24**, 25 (2004).
- [68] W. J. Nellis, N. C. Holmes, A. C. Mitchell, D. C. Hamilton, and M. Nicol, Equation of state and electrical conductivity of “synthetic Uranus,” a mixture of water, ammonia, and isopropanol, at shock pressure up to 200 GPa (2 Mbar), *J. Chem. Phys.* **107**, 9096 (1997).

- [69] A. C. Mitchell and W. J. Nellis, Equation of state and electrical conductivity of water and ammonia shocked to the 100 GPa (1 Mbar) pressure range, *J. Chem. Phys.* **76**, 6273 (1982).
- [70] W. J. Nellis, D. C. Hamilton, N. C. Holmes, H. B. Radousky, F. H. Ree, A. C. Mitchell, and M. Nicol, The nature of the interior of Uranus based on studies of planetary ices at high dynamic pressure, *Science* **240**, 779 (1988).
- [71] W. J. Nellis, A. C. Mitchell, P. C. McCandless, D. J. Erskine, and S. T. Weir, Electronic energy gap of molecular hydrogen from electrical conductivity measurements at high shock pressures, *Phys. Rev. Lett.* **68**, 2937 (1992).
- [72] W. J. Nellis, S. T. Weir, and A. C. Mitchell, Minimum metallic conductivity of fluid hydrogen at 140 GPa (1.4 Mbar), *Phys. Rev. B* **59**, 3434 (1999).
- [73] W. Nellis, Dynamic compression of materials: Metallization of fluid hydrogen at high pressures, *Rep. Prog. Phys.* **69**, 1479 (2006).
- [74] W. J. Nellis, D. C. Hamilton, and A. C. Mitchell, Electrical conductivities of methane, benzene, and polybutene shock compressed to 60 GPa (600 kbar), *J. Chem. Phys.* **115**, 1015 (2001).
- [75] A. A. Golyshev, D. V. Shakhrai, V. V. Kim, A. M. Molodets, and V. E. Fortov, High-temperature resistivity of shocked liquid sodium at pressures up to 230 GPa, *Phys. Rev. B* **83**, 094114 (2011).
- [76] Y. Bi, H. Tan, and F.-Q. Jing, Electrical conductivity of  $\epsilon$ -iron under shock compression up to 208 GPa, *Chin. Phys. Lett.* **19**, 243 (2002).
- [77] Y. Bi, H. Tan, and F. Jing, Electrical conductivity of iron under shock compression up to 200 GPa, *J. Phys.: Condens. Matter* **14**, 10849 (2002).
- [78] A. M. Molodets and A. A. Golyshev, Thermal conductivity of indium at high pressures and temperatures under shock compression, *Phys. Solid State* **51**, 226 (2009).
- [79] M. Bastea and S. Bastea, Electrical conductivity of lithium at megabar pressures, *Phys. Rev. B* **65**, 193104 (2002).
- [80] S. D. Gilev, Electrical conductivity of copper powders under shock compression, *Combust. Explos. Shock Waves* **49**, 359 (2013).
- [81] J. Y. Wong, R. K. Linde, and P. S. D. Carli, Dynamic electrical resistivity of iron: Evidence for a new high pressure phase, *Nature (London)* **219**, 713 (1968).
- [82] P. J. A. Fuller and J. H. Price, Electrical conductivity of manganin and iron at high pressures, *Nature (London)* **193**, 262 (1962).
- [83] A. C. Mitchell and R. N. Keeler, Technique for accurate measurement of the electrical conductivity of shocked fluids, *Rev. Sci. Instrum.* **39**, 513 (1968).
- [84] R. N. Keeler and A. C. Mitchell, Electrical conductivity, demagnetization, and the high-pressure phase transition in shock-compressed iron, *Solid State Commun.* **7**, 271 (1969).
- [85] R. S. Crum, D. A. Brantley, V. Tran, M. C. Akin, and R. Chau, Electrical conductivity of Sn at high pressure and temperature, *Phys. Rev. B* **104**, 184117 (2021).
- [86] D. Kim, J. Bang, P. Won, Y. Kim, J. Jung, J. Lee, J. Kwon, H. Lee, S. Hong, N. L. Jeon *et al.*, Biocompatible cost-effective electrophysiological monitoring with oxidation-free Cu–Au core-shell nanowire, *Adv. Mater. Technol.* **5**, 2000661 (2020).
- [87] R. A. Matula, Electrical resistivity of copper, gold, palladium, and silver, *J. Phys. Chem. Ref. Data* **8**, 1147 (1979).
- [88] A. Lanzillo Nicholas, B. Thomas Jay, B. Watson, M. Washington, and K. Nayak Saroj, Pressure-enabled phonon engineering in metals, *Proc. Natl. Acad. Sci. USA* **111**, 8712 (2014).
- [89] M. A. Gulevich, Measurement of electrical conductivity of copper under impulsive loading, *Combust. Explos. Shock Waves* **47**, 715 (2011).
- [90] S. D. Gilev and V. S. Prokop'ev, Electrical resistance of copper under shock compression: Experimental data, *Combust. Explos. Shock Waves* **52**, 107 (2016).
- [91] S. Y. Savrasov and D. Y. Savrasov, Electron-phonon interactions and related physical properties of metals from linear-response theory, *Phys. Rev. B* **54**, 16487 (1996).
- [92] N. Q. Hoc, B. D. Tinh, and N. D. Hien, Influence of temperature and pressure on the electrical resistivity of gold and copper up to 1350 K and 100 GPa, *Mater. Res. Bull.* **128**, 110874 (2020).
- [93] See Supplemental Material at <http://link.aps.org/supplemental/10.1103/PhysRevB.109.115129> for details of the shock compression and DAC experimental setup and theoretical simulations, the fitted parameters for the Bloch-Grüneisen formula, and the thermal conductivity of Cu at high  $P$ - $T$  conditions.
- [94] H. K. Mao, J. Xu, and P. M. Bell, Calibration of the ruby pressure gauge to 800 kbar under quasi-hydrostatic conditions, *J. Geophys. Res.: Solid Earth* **91**, 4673 (1986).
- [95] H. Gomi, K. Hirose, H. Akai, and Y. Fei, Electrical resistivity of substitutionally disordered hcp Fe–Si and Fe–Ni alloys: Chemically-induced resistivity saturation in the Earth's core, *Earth Planet. Sci. Lett.* **451**, 51 (2016).
- [96] A. Dewaele, P. Loubeyre, and M. Mezouar, Equations of state of six metals above 94 GPa, *Phys. Rev. B* **70**, 094112 (2004).
- [97] A. D. Chijioke, W. J. Nellis, and I. F. Silvera, High-pressure equations of state of Al, Cu, Ta, and W, *J. Appl. Phys.* **98**, 073526 (2005).
- [98] F. M. Smits, Measurement of sheet resistivities with the four-point probe, *Bell Syst. Tech. J.* **37**, 711 (1958).
- [99] Y. Zhang, T. Sekine, and H. He, A new interpretation of decomposition products of serpentine under shock compression, *Am. Mineral.* **99**, 2374 (2014).
- [100] S. P. Marsh, *LASL Shock Hugoniot Data* (University of California Press, Berkeley, 1980).
- [101] A. C. Mitchell and W. J. Nellis, Shock compression of aluminum, copper, and tantalum, *J. Appl. Phys.* **52**, 3363 (1981).
- [102] R. G. Kraus, J. P. Davis, C. T. Seagle, D. E. Fratanduono, D. C. Swift, J. L. Brown, and J. H. Eggert, Dynamic compression of copper to over 450 GPa: A high-pressure standard, *Phys. Rev. B* **93**, 134105 (2016).
- [103] A. Ostriker and D. Nikolaev, Shock induced melting of sapphire, *J. Phys. Conf. Ser.* **2154**, 012010 (2022).
- [104] G. Shen and P. Lazor, Measurement of melting temperatures of some minerals under lower mantle pressures, *J. Geophys. Res.: Solid Earth* **100**, 17699 (1995).
- [105] Z. Wang, H. Mao, and S. K. Saxena, The melting of corundum ( $\text{Al}_2\text{O}_3$ ) under high pressure conditions, *J. Alloys Compd.* **299**, 287 (2000).
- [106] H. Tan, C. D. Dai, L. Y. Zhang, and C. H. Xu, Method to determine the melting temperatures of metals under megabar shock pressures, *Appl. Phys. Lett.* **87**, 221905 (2005).

- [107] C. Dai, H. Tan, and H. Geng, Model for assessing the melting on Hugoniot of metals: Al, Pb, Cu, Mo, Fe, and U, *J. Appl. Phys.* **92**, 5019 (2002).
- [108] W. J. Nellis, A. C. Mitchell, and D. A. Young, Equation-of-state measurements for aluminum, copper, and tantalum in the pressure range 80–440 GPa (0.8–4.4 Mbar), *J. Appl. Phys.* **93**, 304 (2002).
- [109] D. Errandonea, High-pressure melting curves of the transition metals Cu, Ni, Pd, and Pt, *Phys. Rev. B* **87**, 054108 (2013).
- [110] S. Japel, B. Schwager, R. Boehler, and M. Ross, Melting of copper and nickel at high pressure: The role of *d* electrons, *Phys. Rev. Lett.* **95**, 167801 (2005).
- [111] L. Vočadlo, D. Alfè, G. D. Price, and M. J. Gillan, *Ab initio* melting curve of copper by the phase coexistence approach, *J. Chem. Phys.* **120**, 2872 (2004).
- [112] Y. N. Wu, L. P. Wang, Y. S. Huang, and D. M. Wang, Melting of copper under high pressures by molecular dynamics simulation, *Chem. Phys. Lett.* **515**, 217 (2011).
- [113] R. Kubo, Statistical-mechanical theory of irreversible processes. I. General theory and simple applications to magnetic and conduction problems, *J. Phys. Soc. Jpn.* **12**, 570 (1957).
- [114] D. A. Greenwood, The Boltzmann equation in the theory of electrical conduction in metals, *Proc. Phys. Soc.* **71**, 585 (1958).
- [115] G. V. Chester and A. Thellung, The law of Wiedemann and Franz, *Proc. Phys. Soc.* **77**, 1005 (1961).
- [116] J. Zeng, D. Zhang, D. Lu, P. Mo, Z. Li, Y. Chen, M. Rynik, L. Huang, Z. Li, S. Shi *et al.*, DeePMD-kit v2: A software package for deep potential models, *J. Chem. Phys.* **159**, 054801 (2023).
- [117] H. Wang, L. Zhang, J. Han, and E. W., DeePMD-kit: A deep learning package for many-body potential energy representation and molecular dynamics, *Comput. Phys. Commun.* **228**, 178 (2018).
- [118] L. Zhang, J. Han, H. Wang, R. Car, and E. W., Deep potential molecular dynamics: A scalable model with the accuracy of quantum mechanics, *Phys. Rev. Lett.* **120**, 143001 (2018).
- [119] G. Kresse and J. Furthmüller, Efficient iterative schemes for *ab initio* total-energy calculations using a plane-wave basis set, *Phys. Rev. B* **54**, 11169 (1996).
- [120] P. E. Blöchl, Projector augmented-wave method, *Phys. Rev. B* **50**, 17953 (1994).
- [121] G. Kresse and D. Joubert, From ultrasoft pseudopotentials to the projector augmented-wave method, *Phys. Rev. B* **59**, 1758 (1999).
- [122] J. P. Perdew, A. Ruzsinszky, G. I. Csonka, O. A. Vydrov, G. E. Scuseria, L. A. Constantin, X. Zhou, and K. Burke, Restoring the density-gradient expansion for exchange in solids and surfaces, *Phys. Rev. Lett.* **100**, 136406 (2008).
- [123] W. G. Hoover, A. J. C. Ladd, and B. Moran, High-strain-rate plastic flow studied via nonequilibrium molecular dynamics, *Phys. Rev. Lett.* **48**, 1818 (1982).
- [124] D. Lu, W. Jiang, Y. Chen, L. Zhang, W. Jia, H. Wang, and M. Chen, DP Compress: A model compression scheme for generating efficient deep potential models, *J. Chem. Theory Comput.* **18**, 5559 (2022).
- [125] S. Plimpton, Fast parallel algorithms for short-range molecular dynamics, *J. Comput. Phys.* **117**, 1 (1995).
- [126] W. G. Hoover, Canonical dynamics: Equilibrium phase-space distributions, *Phys. Rev. A* **31**, 1695 (1985).
- [127] S. Nosé, A unified formulation of the constant temperature molecular dynamics methods, *J. Chem. Phys.* **81**, 511 (1984).
- [128] C. Di Paola, F. Macheda, S. Laricchia, C. Weber, and N. Bonini, First-principles study of electronic transport and structural properties of Cu<sub>12</sub>Sb<sub>4</sub>S<sub>13</sub> in its high-temperature phase, *Phys. Rev. Res.* **2**, 033055 (2020).
- [129] E. Y. Tonkov and E. G. Ponyatovsky, *Phase Transformations of Elements Under High Pressure* (CRC Press, Boca Raton, 2004).
- [130] Y. Wang, D. Chen, and X. Zhang, Calculated equation of state of Al, Cu, Ta, Mo, and W to 1000 GPa, *Phys. Rev. Lett.* **84**, 3220 (2000).
- [131] J. Li, Q. Wu, J. Li, T. Xue, Y. Tan, X. Zhou, Y. Zhang, Z. Xiong, Z. Gao, and T. Sekine, Shock melting curve of iron: A consensus on the temperature at the Earth's inner core boundary, *Geophys. Res. Lett.* **47**, e2020GL087758 (2020).
- [132] B. Gan, J. Li, Q. Wu, G. Jiang, H. Y. Geng, Y. Tan, X. Zhou, T. Sekine, Z. Gao, and Y. Zhang, Shock temperatures and melting curve of an Fe–Ni–Cr alloy up to 304 GPa, *J. Appl. Phys.* **131**, 045901 (2022).
- [133] Y. Zhang, Y. Tan, H. Y. Geng, N. P. Salke, Z. Gao, J. Li, T. Sekine, Q. Wang, E. Greenberg, V. B. Prakapenka *et al.*, Melting curve of vanadium up to 256 GPa: Consistency between experiments and theory, *Phys. Rev. B* **102**, 214104 (2020).
- [134] Y. N. Zhugin and Y. L. Levakova, Effect of the conductance and thickness of a conducting plate on the signal from a material-velocity inductive transducer, *J. Appl. Mech. Tech. Phys.* **41**, 1136 (2000).
- [135] R. Stevens and J. Boerio-Goates, Heat capacity of copper on the ITS-90 temperature scale using adiabatic calorimetry, *J. Chem. Thermodynamics* **36**, 857 (2004).
- [136] A. Bid, A. Bora, and A. K. Raychaudhuri, Temperature dependence of the resistance of metallic nanowires of diameter  $\geq 15$  nm: Applicability of Bloch-Grüneisen theorem, *Phys. Rev. B* **74**, 035426 (2006).
- [137] W. B. Holzapfel, M. Hartwig, and W. Sievers, Equations of state for Cu, Ag, and Au for wide ranges in temperature and pressure up to 500 GPa and above, *J. Phys. Chem. Ref. Data* **30**, 515 (2001).
- [138] O. Gunnarsson, M. Calandra, and J. E. Han, Colloquium: Saturation of electrical resistivity, *Rev. Mod. Phys.* **75**, 1085 (2003).
- [139] R. Franz and G. Wiedemann, Ueber die Wärme-Leitungsfähigkeit der Metalle, *Ann. Phys.* **165**, 497 (1853).
- [140] J. P. Moore, D. L. McElroy, and R. S. Graves, Thermal conductivity and electrical resistivity of high-purity copper from 78 to 400 °K, *Can. J. Phys.* **45**, 3849 (1967).
- [141] B. Giordanengo, N. Benazzi, J. Vinckel, J. G. Gasser, and L. Roubi, Thermal conductivity of liquid metals and metallic alloys, *J. Non-Cryst. Solids* **250–252**, 377 (1999).
- [142] H. Gomi and T. Yoshino, Impurity resistivity of fcc and hcp Fe-based alloys: Thermal stratification at the top of the core of super-Earths, *Front. Earth Sci.* **6**, 217 (2018).
- [143] Z. Lin, L. V. Zhigilei, and V. Celli, Electron-phonon coupling and electron heat capacity of metals under conditions of strong electron-phonon nonequilibrium, *Phys. Rev. B* **77**, 075133 (2008).